A&A 665, A46 (2022)
https://doi.org/10.1051/0004-6361/202243609

Astronomy & Astrophysics

High-precision chemical abundances of Galactic building blocks

II. Revisiting the chemical distinctness of the Helmi streams*

Tadafumi Matsuno[1], Emma Dodd[1], Helmer H. Koppelman[2], Amina Helmi[1], Miho N. Ishigaki[3], Wako Aoki[3], Jingkun Zhao[4], Zhen Yuan[5], and Kohei Hattori[3,6]

[1] Kapteyn Astronomical Institute, University of Groningen, Landleven 12, 9747 AD Groningen, The Netherlands
e-mail: matsuno@astro.rug.nl
[2] School of Natural Sciences, Institute for Advanced Study, 1 Einstein Drive, Princeton, NJ 08540, USA
[3] National Astronomical Observatory of Japan, 2-21-1 Osawa, Mitaka, Tokyo 181-8588, Japan
[4] Key Lab of Optical Astronomy, National Astronomical Observatories, Chinese Academy of Sciences, A20 Datun Road, Chaoyang, Beijing 100101, PR China
[5] Université de Strasbourg, CNRS, Observatoire Astronomique de Strasbourg, UMR 7550, 67000 Strasbourg, France
[6] Institute of Statistical Mathematics, 10-3 Midoricho, Tachikawa, Tokyo 190-0014, Japan

Received 22 March 2022 / Accepted 1 June 2022

ABSTRACT

Context. The Helmi streams are a kinematic substructure whose progenitor is likely a dwarf galaxy. Although 20 years have passed since their discovery, it is still unclear whether their members are chemically distinguishable from other halo stars in the Milky Way.
Aims. We aim to precisely characterize the chemical properties of the Helmi streams.
Methods. We analyzed high-resolution, high signal-to-noise ratio spectra for 11 Helmi stream stars through a line-by-line abundance analysis. We compared the derived abundances to homogenized literature abundances of the other halo stars, including those belonging to other kinematic substructures, such as *Gaia*-Enceladus and Sequoia.
Results. Compared to typical halo stars, the Helmi stream members clearly show low values of [X/Fe] in elements produced by massive stars, such as Na and α-elements. This tendency is seen down to metallicities of at least [Fe/H] ~ -2.2, suggesting type Ia supernovae already started to contribute to the chemical evolution at this metallicity. We find that the [α/Fe] ratio does not evolve significantly with metallicity, making the Helmi stream stars less distinguishable from *Gaia*-Enceladus stars at [Fe/H] $\gtrsim -1.5$. The almost constant but low value of [α/Fe] might be indicative of quiescent star formation with low efficiency at the beginning and bursty star formation at later times. We also find extremely low values of [Y/Fe] at low metallicity, providing further support for the claim that light neutron-capture elements are deficient in Helmi streams. While Zn is deficient at low metallicity, it shows a large spread at high metallicity. The origin of the extremely low Y abundances and Zn variations remains unclear.
Conclusions. The Helmi stream stars are distinguishable from the majority of the halo stars if homogeneously derived abundances are compared.

Key words. Galaxy: abundances – Galaxy: halo – stars: abundances – Galaxy: stellar content

1. Introduction

The Helmi streams were discovered by Helmi et al. (1999) as a kinematic substructure among halo stars, which is an expected signature of past galaxy accretion. They were thus one of the first pieces of evidence for the hierarchical formation of the Milky Way expected from the standard cosmology. The streams were discovered as an overdensity in the plane of angular momenta in a sample of <100 low-metallicity stars. Later studies also confirmed their existence (Chiba & Beers 2000; Kepley et al. 2007; Myeong et al. 2018; Koppelman et al. 2018). Their progenitor was likely a dwarf galaxy with a stellar mass of $\sim 10^8\,M_\odot$ and a mean metallicity of [Fe/H] ~ -1.5 that was accreted to the Milky Way around 5−8 Gyr ago (Kepley et al. 2007; Koppelman et al. 2019).

Even though the streams were discovered more than 20 years ago, their chemical properties have not received much attention until recently. Roederer et al. (2010) studied the chemical abundances of 12 stars in the stream, concluding that the stars have similar abundance ratios as the rest of the halo stars. In recent years, Limberg et al. (2021), Gull et al. (2021), Aguado et al. (2021), and Nissen et al. (2021) conducted chemical analysis for the Helmi stream members. While Gull et al. (2021) reach the same conclusion as Roederer et al. (2010), the other studies hint at possible chemical peculiarities of the streams. For example, the Sr abundance seems to be much lower than typical for halo stars at [Fe/H] $\lesssim -2$ (Aguado et al. 2021); two stars in a binary system in the Helmi streams, namely G112-43 and G112-44, have enhanced ratios of [Mn/Fe], [Ni/Fe], [Cu/Fe], ande [Zn/Fe] compared to other accreted stars in the Milky Way (Nissen et al. 2021); and the [α/Fe] ratio seems to be decreasing at [Fe/H] $\gtrsim -2$ (Limberg et al. 2021; Aguado et al. 2021).

Many of the previous comparisons made use of heterogeneous literature compilation. They were therefore limited by systematic uncertainties, which can be as large as 0.4 dex in [Fe/H] and 0.2 dex in [X/Fe]. This can easily obscure or falsely create abundance peculiarities, as we will see later in this paper. Another complication arises because the literature sample was often a mixture of accreted and in situ stars. As

* Full Table 5 is only available at the CDS via anonymous ftp to cdsarc.u-strasbg.fr (130.79.128.5) or via http://cdsarc.u-strasbg.fr/viz-bin/cat/J/A+A/665/A46

Table 1. Summary of the data.

Object	*Gaia* EDR3 source id	$S/N_{4500\,Å}$	$S/N_{5533\,Å}$	$S/N_{6370\,Å}$
2447_5952	2447968154259005952	80	108	173
4998_5552	4998741805354135552	72	83	78
6170_9904	6170808423037019904	87	88	77
6615_9776	6615661065172699776	97	161	122
6914_3008	6914409197757803008	73	86	120
J1306+4154	1527475951701753984	50	65	53
J1436+0929	1176187720407158912	134	110	91
J1553+3909	1376687518318241536	84	73	55
J1730+5309	1416077522383596160	84	63	42
J1642+2041	4564066449004092928	63	60	86
LP894-3	2891152566675457280	97	150	143

Notes. We obtained new high-resolution spectra for all objects except LP894-3. The signal-to-noise ratios are converted to per 0.01 Å.

Nissen & Schuster (2010, hereafter, NS10) showed from their homogeneously analyzed samples, the Milky Way halo contains two major populations, accreted and in situ stars, which differ in abundance ratios. Without understanding the origin of the comparison sample, it remains unclear if the chemical peculiarities of the Helmi stream stars, if any, indicate simply that they are accreted or that the progenitor had a unique evolution. Nissen et al. (2021) is the only exception in the sense that they compared Helmi stream members with accreted stars using homogeneously derived chemical abundance. However, larger samples could aid our understanding of the interesting abundance pattern reported in the two stars in a binary system.

Throughout this study, we aim to precisely characterize the chemical abundances of the Helmi stream stars and to compare them with homogeneous abundances of other components in the Milky Way halo, including *Gaia*-Enceladus, in situ stars (NS10; Reggiani et al. 2017, hereafter R17), and Sequoia (Matsuno et al. 2022, hereafter, Paper I). The precise chemical abundance ratios tell us about the progenitor's properties, but the chemical distinctness of kinematic substructures, if found, would also enable us to "chemically tag" stars originating from the same progenitor. In Paper I, we show that a combination of a line-by-line abundance analysis for a carefully selected sample and homogenization of literature abundances using standard stars is a powerful way to precisely characterize the chemical properties of kinematic substructures.

We studied the chemical abundance of the Helmi stream stars in the same way as in Paper I. Namely, we analyzed high signal-to-noise ratio spectra for 11 stars in the Helmi streams, measured their chemical abundance through a line-by-line analysis with careful treatment of uncertainty, and compared them with other halo stars in NS10 and R17 after homogenizing all the abundances. We describe the observation, data reduction, targets, and stars in the literature in Sect. 2. In Sect. 3, after briefly explaining our approach for the chemical abundance measurement and homogenization, we present chemical abundance ratios of the Helmi stream stars. After providing discussions in Sect. 4, we summarize our findings in Sect. 5.

2. Data

2.1. Observation

We obtained high-resolution spectra for ten stars with the High Dispersion Spectrograph (Noguchi et al. 2002) on the Subaru telescope[1]. The selection and properties of the targets are described in the following subsection. The observations were conducted on August 9-10, 2020, with the standard setup of the HDS (StdYd), which yields a wavelength coverage from ∼4000 Å to ∼6800 Å. We used the image slicer #2 (Tajitsu et al. 2012), which provides a resolving power of $R \sim 80\,000$. The data reduction was performed using an `IRAF` script[2], `hdsql`[3], including CCD linearity correction, scattered light subtraction, aperture extraction, flat-fielding, wavelength calibration, and heliocentric velocity correction. Information about the spectra is summarized in Table 1.

We also searched archives for high signal-to-noise ratio and high-resolution spectra for stars that satisfy our selection criteria described in the following subsection. We find that LP894-3 satisfies our selection and has spectra in the Subaru telescope archive. We, therefore, analyzed the archival spectrum of this star. The spectrum used is the same as that used by Ishigaki et al. (2012).

2.2. Targets

Targets were selected based on the orbital angular momenta of the stars following Koppelman et al. (2019). Namely, the selection box was defined with the component of the angular momentum along the z-axis of the Milky Way (L_z) and $L_{\rm perp}$, which is given by $\sqrt{L_x^2 + L_y^2}$. We also restricted our sample to those around the turn-off region using *Gaia* DR2 photometry. The exact selection criteria were $1000 < L_z/{\rm kpc\,km\,s^{-1}} < 1500$ and $1750 < L_{\rm perp}/{\rm kpc\,km\,s^{-1}} < 2600$ (the kinematic selection, corresponding to the box A of Koppelman et al. 2019), and $0.5 < G_{BP} - G_{RP} < 0.95$ and $3.2 < G_{\rm abs} < 5.8$ (the color-magnitude selection), where G_{BP}, G_{RP}, and $G_{\rm abs}$ are *Gaia BP* and *RP* magnitude, and the absolute magnitude in the *Gaia G* band, respectively.

Initially, for the target selection, we used *Gaia* DR2 astrometry, photometry, and radial velocity (Gaia Collaboration 2018),

[1] *Gaia* EDR3 1909569058536197760 was also observed but not analyzed since it is a double-lined spectroscopic binary.
[2] IRAF is distributed by the National Optical Astronomy Observatory, which is operated by the Association of Universities for Research in Astronomy (AURA) under a cooperative agreement with the National Science Foundation.
[3] http://www.subarutelescope.org/Observing/Instruments/HDS/hdsql-e.html

Table 2. Property of the targets.

Object	π (mas)	$\sigma(\pi)$ (mas)	G (mag)	$B_p - R_p$ (mag)	$E(B-V)$ (mag)	RV (km s^{-1})
2447_5952	2.817	0.021	11.963	0.677	0.096	145.5
4998_5552	3.463	0.018	12.561	0.784	0.000 [(a)]	−187.6
6170_9904	3.743	0.018	10.573	0.728	0.064	−122.4
6615_9776	4.984	0.014	12.064	0.768	0.010	−276.9
6914_3008	3.195	0.017	12.622	0.720	0.015	113.9
J1306+4154	1.470	0.013	13.499	0.668	0.046	−294.7
J1436+0929	3.294	0.019	12.172	0.671	0.006	−301.4
J1553+3909	1.944	0.013	13.619	0.741	0.018	−288.3
J1642+2041	0.997	0.013	13.479	0.765	0.070	−246.3
J1730+5309	0.751	0.011	13.967	0.817	0.082	70.9
LP894-3	5.347	0.038	11.090	0.710	0.010	303.0 [(b)]

Notes. [(a)]This object is not covered by Green et al. (2019). Since Schlegel et al. (1998) provide $E(B-V) = 0.01$ and since this object is nearby, we assumed $E(B-V) = 0.0$ for this object. [(b)]From Ishigaki et al. (2012).

Table 3. Kinematics of the targets.

Object	v_z (km s^{-1})	$\sigma(v_z)$ (km s^{-1})	L_z (kpc km s^{-1})	$\sigma(L_z)$ (kpc km s^{-1})	$L_{\rm perp}$ (kpc km s^{-1})	$\sigma(L_{\rm perp})$ (kpc km s^{-1})	$E/10^5$ (km^2 s^{-2})	$\sigma(E)/10^5$ (km^2 s^{-2})	Subclass [(a)]
2447_5952	−216.7	1.1	1278	11	1872	9	−1.022	0.007	...
4998_5552	230.1	1.1	1020	6	1846	9	−1.429	0.002	...
6170_9904	−272.8	1.3	1200	9	2201	11	−1.342	0.003	hiL
6615_9776	213.8	0.9	1345	2	1757	8	−1.339	0.003	loL
6914_3008	−283.9	1.5	1437	8	2279	12	−1.275	0.004	hiL
J1306+4154	−281.3	0.9	1288	2	2363	7	−1.293	0.002	hiL
J1436+0929	−249.4	0.9	1226	4	2050	7	−1.312	0.003	hiL
J1553+3909	−268.6	0.8	1304	6	2208	7	−1.299	0.002	hiL
J1642+2041	−217.0	1.2	1339	7	1737	9	−1.392	0.003	loL
J1730+5309	238.3	2.4	1423	14	1965	19	−1.384	0.004	loL
LP894−3	−219.8	0.7	1015	6	1813	6	−1.283	0.003	...

Notes. [(a)]Subclass defined by Dodd et al. (2022). In the last column, "hiL" indicates a clump with a higher $L_{\rm perp}$ and "loL" one with a lower $L_{\rm perp}$.

and Large Sky Area Multi-Object Fiber Spectroscopic Telescope (LAMOST) survey DR5 radial velocity. We assumed $U_\odot = -11.1$ km s^{-1}, $W_\odot = 7.3$ km s^{-1} (Schönrich et al. 2010), $R_0 = 8.21$ kpc (McMillan 2017), and $z_0 = 20.8$ pc (Bennett & Bovy 2019) for the solar velocity and position. Adopting the proper motion measurement for Sgr A* (Reid & Brunthaler 2004), we assumed the sun is moving at 245.3 km s^{-1} in the direction of the Galactic rotation. When calculating the orbital energies of the stars, we adopted the Milky Way potential of McMillan (2017).

Information about the kinematic and photometric properties of the targets is summarized in Tables 2 and 3, and visualized in Figs. 1 and 2. We note that we updated the kinematic and photometric information with *Gaia* EDR3 photometry and astrometry (Gaia Collaboration 2021). The radial velocities were also updated to the values we measured from our high-resolution spectra by comparing the observed wavelengths of neutral Fe lines with those from laboratory experiments.

Table 3 also includes information about subgroups among the Helmi stream stars. We consider here two ways of subdividing the Helmi stream stars. One is by the sign of v_z; Kepley et al. (2007) and Koppelman et al. (2019) used the asymmetry in the number of stars in each subgroup to estimate the accretion time of the progenitor of the Helmi streams. Another subdivision follows that by Dodd et al. (2022) in the space of L_z and $L_{\rm perp}$. They show that these two groups of stars with slightly different kinematics reflect the effect of an orbital resonance in the Milky Way potential. In either definition, the two subgroups are considered parts of the same substructure, the Helmi streams. In all figures, symbols are hatched according to the subdivision by Dodd et al. (2022).

2.3. Literature

We compared the chemical abundance of the Helmi stream stars with those in literature. Since our approach described in Sect. 3 is identical to that used in Paper I, we can naturally compare our abundance in the present study with *Gaia*-Enceladus and in situ stars from NS10 and R17 and with Sequoia stars from Paper I. Since abundances from these studies were homogenized using standard stars (see Paper I), precise comparisons are possible. We refer to Paper I for more details.

Among the stars studied by NS10 and R17, we find two stars that satisfy our kinematic selection criteria for the Helmi streams. These two stars are G112-43 and G112-44 and were studied in detail by Nissen et al. (2021) as part of the Helmi streams. Although they are considered to form a binary system,

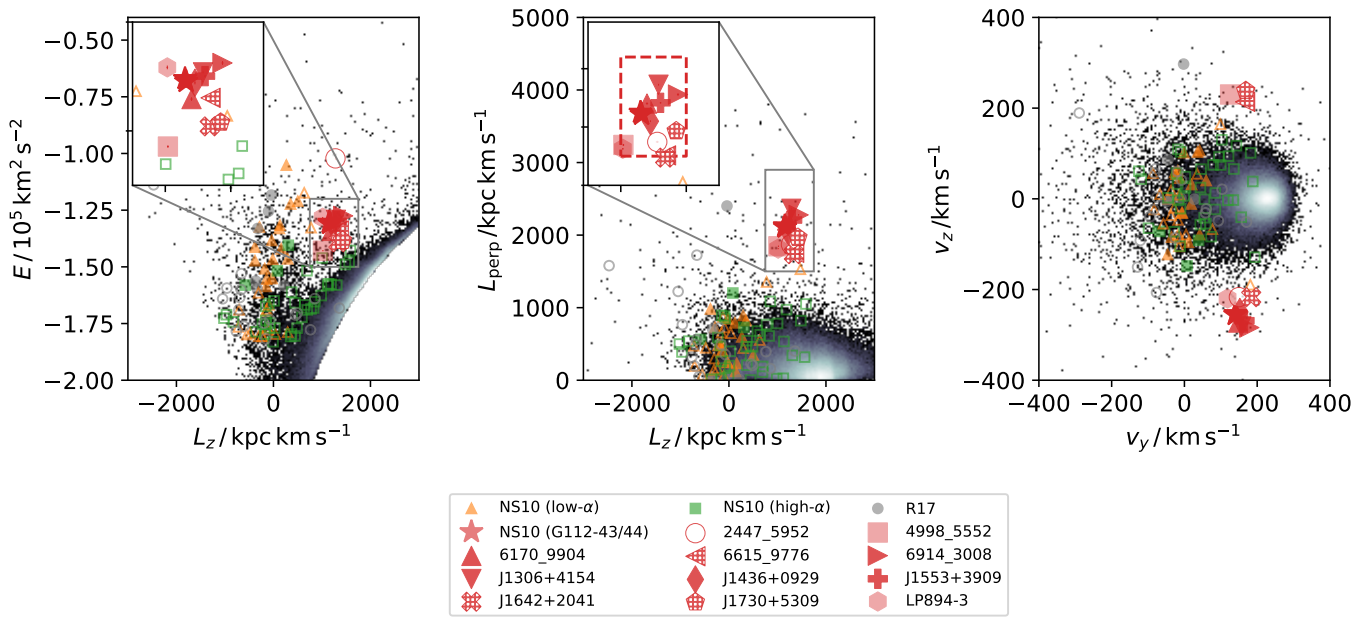

Fig. 1. Distribution of stars in kinematic spaces, namely $E - L_z$, $L_{\mathrm{perp}} - L_z$, and $v_y - v_z$. The insets in the left two panels show better distribution of the stars that are part of the Helmi streams. The Helmi stream selection from Koppelman et al. (2019) is shown as a dashed box in the inset of the *middle panel*. Stars are hatched according to the subgroups found by Dodd et al. (2022). Three stars (2447_5952, 4998_5552, and LP894-3) are not associated with either of the subgroups. An open symbol is assigned only to 2447_5952 since it has much larger energy than the other Helmi stream stars. We used filled symbols for stars from NS10 and R17 if they satisfy the kinematic selection for *Gaia*-Enceladus (see Paper I).

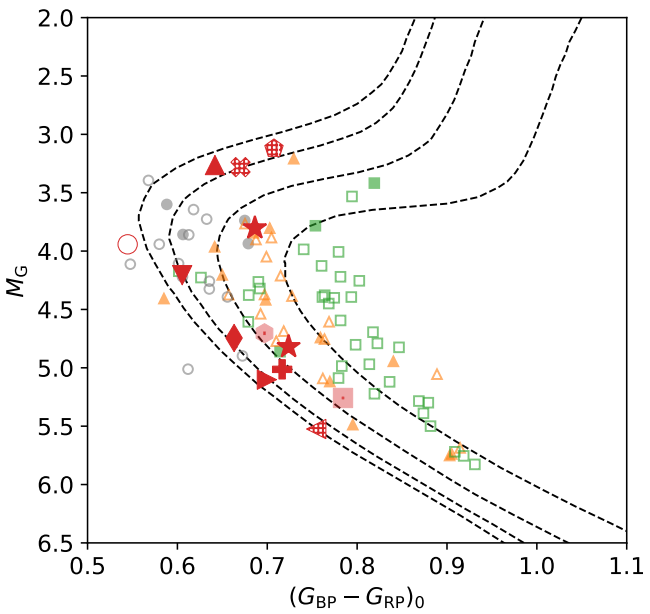

Fig. 2. Location of the stars in the color-magnitude diagram. The symbols follow those of Fig. 1. The four isochrones are from the PARSEC tracks with the age of 12 Gyr and [Fe/H] = −2.0, −1.5, −1.0, and −0.5.

their motions within the system do not affect the estimated orbital properties within the Milky Way since the separation between the two stars is large (>2000 au).

3. Chemical abundances

3.1. Abundance analysis

We provide here a brief description of our analysis, and readers can refer to Paper I for a complete and detailed explanation. The abundance measurements were based on equivalent width measurements, where we assumed a Voigt profile for the line shape. We applied spectral synthesis for Si, Mn, Zn, and Y. Hyperfine structure splitting was considered for Na, Mn, and Ba. Abundances were estimated based on the assumption of local thermodynamic equilibrium (LTE) using MOOG (Sneden 1973) and based on one-dimensional plane-parallel MARCS atmosphere models (Gustafsson et al. 2008). We applied non-LTE corrections of Lind et al. (2011) to the obtained Na abundance through the INSPECT database[4,5].

The effective temperature (T_{eff}) was determined by minimizing the correlation between the excitation potentials and line-by-line abundances of neutral iron lines. The microturbulent velocity (v_t) was determined similarly by minimizing the correlation between reduced equivalent widths and abundances. The surface gravity ($\log g$) was determined from temperature, luminosity, and stellar mass, where the luminosity was obtained by applying a bolometric correction of Casagrande & VandenBerg (2018) to the absolute magnitude in the *Gaia* G band, and mass was derived from isochrone fitting in the color-magnitude diagram. This method of $\log g$ determination has an advantage over the spectroscopic method, requiring the ionization equilibrium between Fe I and Fe II, in that it does not strongly depend on the assumed T_{eff}. For the stellar parameter determination, we used the simple mean of iron abundances derived from individual Fe II lines because Fe II abundances are less affected by the non-LTE effect and temperature uncertainty than Fe I abundances. We took correlated uncertainties into consideration for the esti-

[4] Data obtained from the INSPECT database, version 1.0 (www.inspect-stars.com).

[5] The Na abundances in the comparison literature are in LTE (NS10) and in non-LTE (R17). This inconsistency does not affect our conclusions since we put all the abundances onto the same scale and since NS10 used Na lines that require small non-LTE corrections (≲0.1 dex).

Table 4. Stellar parameters.

Object	$T_{\rm eff}$ (K)	$\sigma(T_{\rm eff})$ (K)	$\log g$ (dex)	$\sigma(\log g)$ (dex)	v_t (km s^{-1})	$\sigma(v_t)$ (km s^{-1})	[Fe/H] (dex)	σ([Fe/H]) (dex)	$\rho_{T_{\rm eff},\log g}$	$\rho_{T_{\rm eff},v_t}$	$\rho_{T_{\rm eff},{\rm [Fe/H]}}$	$\rho_{\log g,v_t}$	$\rho_{\log g,{\rm [Fe/H]}}$	$\rho_{v_t,{\rm [Fe/H]}}$
2447_5952	6275	84	4.195	0.040	1.371	0.101	−1.416	0.028	0.498	0.547	0.263	0.058	0.613	−0.337
4998_5552	5562	57	4.413	0.058	1.022	0.154	−1.282	0.040	0.071	0.695	−0.305	−0.268	0.605	−0.579
6170_9904	5946	72	3.789	0.043	1.251	0.102	−1.706	0.033	0.425	0.605	0.003	0.138	0.389	−0.395
6615_9776	5490	61	4.481	0.033	0.752	0.226	−2.175	0.026	0.440	0.836	−0.540	0.239	0.195	−0.782
6914_3008	5706	69	4.400	0.034	0.821	0.157	−1.730	0.025	0.399	0.836	−0.343	0.128	0.323	−0.500
J1306+4154	6175	108	4.261	0.051	1.272	0.114	−1.211	0.029	0.479	0.696	0.094	0.180	0.583	−0.221
J1436+0929	6109	55	4.374	0.031	1.370	0.104	−1.839	0.038	0.428	0.634	0.012	0.166	0.249	−0.244
J1553+3909	5623	60	4.346	0.036	0.871	0.184	−1.409	0.022	0.405	0.745	−0.526	0.175	0.339	−0.749
J1642+2041	5840	70	3.784	0.089	1.293	0.083	−1.275	0.043	−0.037	0.762	−0.143	−0.446	0.827	−0.501
J1730+5309	5778	59	3.706	0.071	1.245	0.067	−1.661	0.039	−0.024	0.587	−0.021	−0.541	0.776	−0.502
LP894−3	6035	83	4.341	0.038	1.321	0.142	−1.505	0.034	0.561	0.856	0.154	0.387	0.370	0.021

Table 5. Linelist and line-by-line abundance.

Object	Species	λ (Å)	χ (eV)	$\log gf$ (dex)	EW (mÅ)	$\sigma(EW)$ (mÅ)	$A(X)$ (dex)
2447_5952	NaI	5682.633	2.102	−0.706	5.1	0.5	4.675
2447_5952	NaI	5889.959	0.000	−0.193	172.0	8.0	4.558
2447_5952	NaI	5895.910	0.000	−0.575	151.6	7.0	4.505
2447_5952	MgI	4167.271	4.346	−0.746	82.4	3.8	6.385
2447_5952	MgI	4730.040	4.340	−2.379	5.3	0.6	6.472

$\sigma(A)_{T_{\rm eff}}$ (dex)	$\sigma(A)_{\log g}$ (dex)	$\sigma(A)_{v_t}$ (dex)	$\sigma(A)_{\rm [Fe/H]}$ (dex)	$\sigma(A)_{EW}$ (dex)	s_X (dex)	Weight
0.028	0.000	0.000	0.001	0.049	0.000	285.037
0.084	−0.017	−0.015	0.003	0.098	0.000	22.804
0.084	−0.014	−0.020	0.003	0.103	0.000	22.571
0.041	−0.009	−0.007	0.001	0.061	0.000	124.161
0.030	0.000	0.000	0.001	0.055	0.000	170.647

Notes. The full table is available online at the CDS; only a portion of the table is shown here.

mates of uncertainties. The derived parameters are presented in Table 4.

The elemental abundances are the weighted average of the abundances derived from the individual lines. The weights were determined following the prescription by Ji et al. (2020). The weights on individual lines as well as line-by-line abundances and their sensitivities to stellar parameters are summarized in Table 5. When considering [X/Fe], we used the Fe abundance from the same ionization stage as the species X.

All of the analysis was conducted relative to HD59392, for which we adopted $T_{\rm eff}$ = 6012 K, $\log g$ = 3.954, v_t = 1.4 km s^{-1}, and [Fe/H]$_{\rm sp}$ = −1.6 (NS10; Paper I). The elemental abundance of this star was taken from NS10 and Nissen & Schuster (2011). In Paper I, we validated our results using a few standard stars and confirm that our abundances are on the same scale as NS10, Nissen & Schuster (2011) and R17. We note that one of the standard stars was G112-43 in the Helmi streams, for which Nissen & Schuster (2011) and Nissen et al. (2021) reported high Zn abundance. Since we do not find any systematic offset in the derived abundance for this star when comparing with NS10 and Nissen & Schuster (2011), our analysis also confirms its high Zn abundance.

In case no lines were detected for a species, we provided 1-σ and 3-σ upper limits on the abundance, which were estimated from the expected uncertainty on equivalent widths from the equation in Cayrel (1988). We used the Si I line at 6237 Å and the Y II line at 4884 Å to place upper limits. The derived abundances and upper limits are presented in Table A.1.

As an additional test, we investigated the effect of slightly different atmospheric structures due to different α-element abundances in model atmospheres, since the sample includes stars showing different [α/Fe] compared to typical halo stars. We used two MARCS model atmospheres with $T_{\rm eff}$ = 6000 K, $\log g$ = 4.0, v_t = 1.5 km s^{-1}, and [Fe/H] = −1.5 differing in [α/Fe], one of which has the "standard composition" at this metallicity with [α/Fe] = +0.4 and the other has a solar [α/Fe]. Assuming the chemical composition of HD59392, we first computed equivalent widths of absorption lines using the standard α-enhanced model atmosphere. We then derived abundances with the other model from the computed equivalent widths. The maximum difference between the assumed and derived abundances is found in strong lines to be ∼0.02 dex. Since the variation in [α/Fe] among our sample is ∼0.2 dex and since every line is affected in the same direction, the effect of different [α/Fe] in model atmospheres is at most 0.01 dex when discussing [X/H] and even smaller when discussing [X/Fe].

3.2. Results

Figure 3 shows [Na/Fe] and [Mg/Fe] ratios of the Helmi stream stars together with the halo stars from NS10 and R17 and the Sequoia stars from Paper I, all of which are on the same

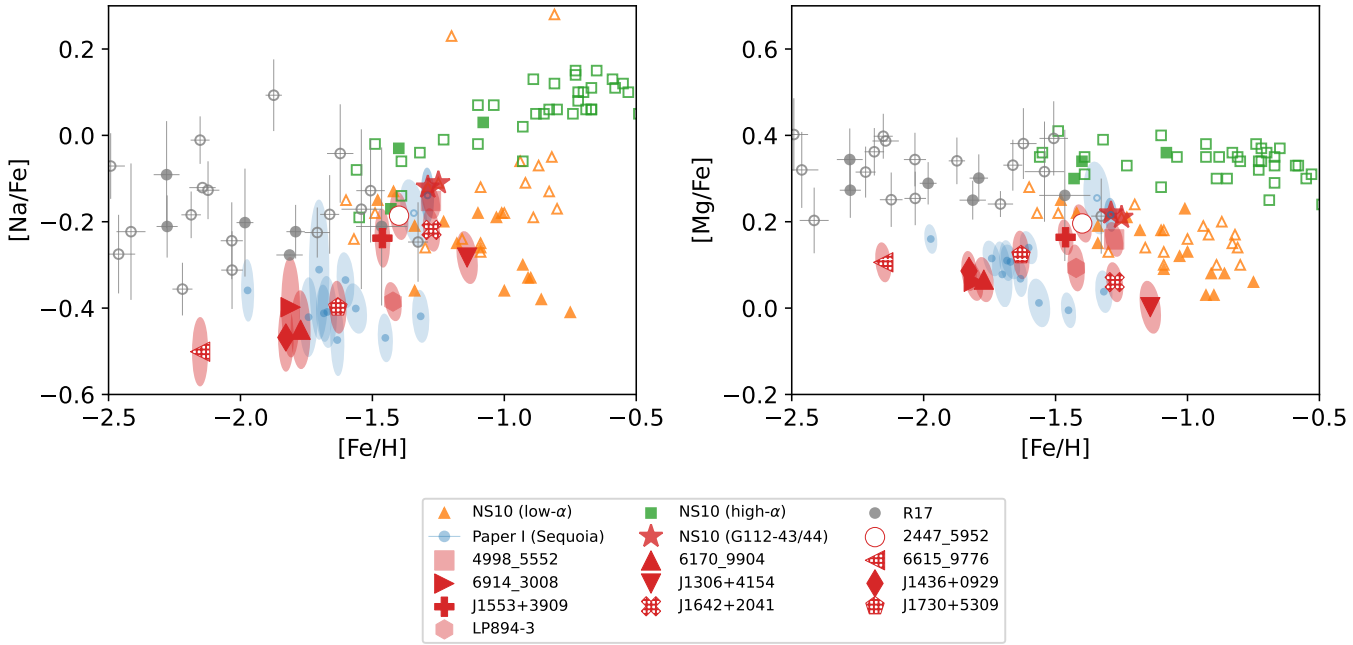

Fig. 3. [Na/Fe] and [Mg/Fe] abundance ratios of the Helmi stream stars (red symbols). Also plotted are halo stars from NS10 and R17, with *Gaia*-Enceladus stars shown with filled symbols. G112-43 and G112-44 from NS10 are shown with red stars since their kinematics are consistent with the Helmi streams. We also show kinematically selected Sequoia stars from Paper I.

abundance scale. We note that we indicate *Gaia*-Enceladus stars in the literature with filled symbols in figures. At $-1.8 \lesssim$ [Fe/H] $\lesssim -1.6$, the Helmi stream stars show similar Na and Mg abundances to Sequoia stars, having clearly lower [Na/Fe] and [Mg/Fe] values compared to other halo stars including *Gaia*-Enceladus stars. The Helmi stream stars with [Fe/H] $\gtrsim -1.5$ also have lower values in these abundance ratios than in situ halo stars. Although they are less separated from *Gaia*-Enceladus stars at this high metallicity, they still tend to show lower [Mg/Fe] values compared to *Gaia*-Enceladus stars. The most metal-poor star 6615_9776 also seems to show a lower abundance of Na and Mg compared to other halo stars. We, however, note that this star is in the metallicity range, [Fe/H] < -2.1, where R17 measured the abundance of stars using a standard star that is different from what they used for stars with [Fe/H] > -2.1. Hence, there is no guarantee that the abundance of 6615_9976 and R17 stars with similar metallicity are on the same scale. Readers can refer to Paper I for the effect of different standard stars (see the results of abundance comparison for HIP28104 in Sect. 3 of Paper I).

Figure 4 shows Si, Ca, and Ti abundances, which are also known to be different between stars with different origins (NS10; Paper I). The behavior of the Helmi stream stars in Ca and Ti is similar to that in Na and Mg; the stars show clearly lower abundance at low metallicity than most halo stars, while they become more indistinguishable from *Gaia*-Enceladus stars at higher metallicity. For Si, the picture is unclear because the Si lines become too weak at [Fe/H] $\lesssim -1.5$.

The observed trends in the α-elements confirm the results of Limberg et al. (2021) and Aguado et al. (2021) in the sense that the Helmi stream stars have lower α-element abundance compared to general Milky Way stars. We added here another important result; the α-element abundances of the Helmi stream stars are even lower than another accreted population, the *Gaia*-Enceladus stars, especially at [Fe/H] $\lesssim -1.5$. Moreover, contrary to the conclusion of Limberg et al. (2021) and Aguado et al. (2021) that the [α/Fe] ratios decrease with metallicity, the evolution in α-elements (Mg, Ca, and Ti) with metallicity observed in the present study is rather flat from [Fe/H] ~ -2.1 to [Fe/H] ~ -1.2. The low α abundance of the Helmi stream stars is also in contrast with Roederer et al. (2010), who concluded that the Helmi stream stars have a similar abundance as other halo stars. We consider that our precise and homogeneous abundance comparisons enable us to detect the abundance difference between the Helmi stream stars and *Gaia*-Enceladus stars and precisely depict the chemical evolutionary track followed by the Helmi streams. We further discuss the importance of the homogeneous abundance analysis in Sect. 4.2.

The abundances of elements near the iron-peak, namely Cr, Mn, Ni, and Zn, are shown in Fig. 5. It has been reported that Cr, Ni and Zn abundances are different between accreted stars and in situ stars (Nissen & Schuster 2011). We, therefore, expect that these abundances are different among the various kinematic substructures with different α-element abundances. We, however, do not see apparent abundance differences between the Helmi stream stars and the other halo stars in Cr and Ni at our measurement uncertainty. On the other hand, Zn appears depleted in the Helmi streams at low metallicity, while there is a large variation at high metallicity. The Helmi stream stars tend to show a low value of [Mn/Fe] at [Fe/H] $\lesssim -1.5$ while they seem to be consistent with typical *Gaia*-Enceladus stars at higher metallicity.

The high Zn abundance of G112-43 and G112-44 was reported in Nissen & Schuster (2011) and confirmed in Nissen et al. (2021). It is also supported for G112-43 by our analysis in Paper I as described in Sect. 3.1. The other Helmi stream stars in the present study, on the other hand, do not share a similar Zn enhancement. We attempt to interpret the Zn abundance evolution of the Helmi streams in Sect. 4.1.

Abundances of neutron-capture elements are shown in Fig. 6. The Helmi stream stars are clearly deficient in Y at low metallicity. This behavior of Y resembles that of Sr reported by Aguado et al. (2021), which is expected since both are light

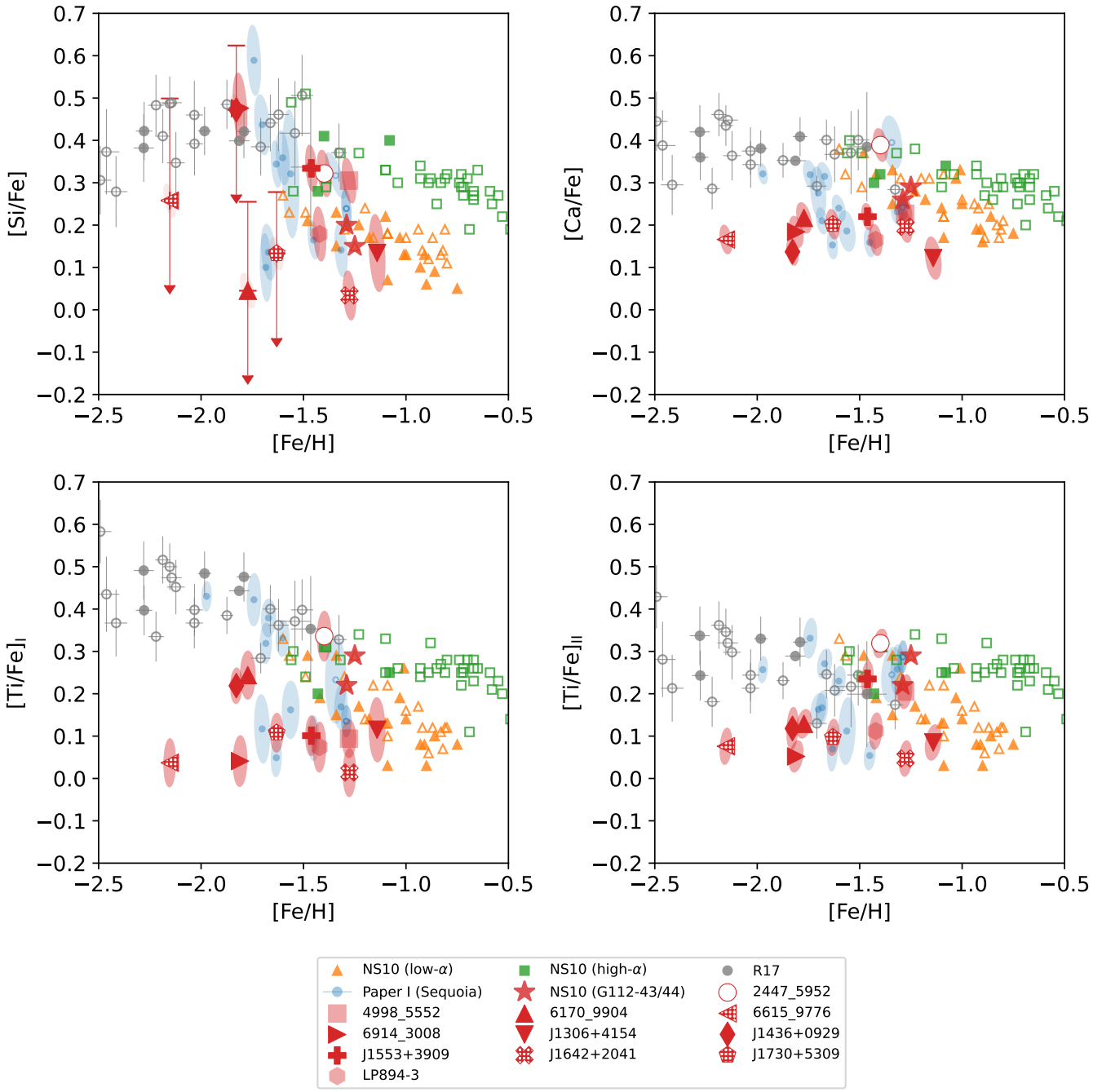

Fig. 4. α-element abundances of the Helmi stream stars. The symbols follow those of Fig. 3. When a star does not have any detectable lines for an element, we indicate the abundances corresponding to the 1-σ and 3-σ upper limits on the equivalent widths, respectively shown with the location of the symbols and the upper end of the error bars.

neutron-capture elements and since these two elements usually show similar trends with [Fe/H]. It is hard to conclude if the Ba abundance evolution of the Helmi streams is distinct from that of *Gaia*-Enceladus or other halo stars because of large scatter. However, we remark that the Helmi stream stars tend to be on the lower side in [Ba/Fe] at given [Fe/H] compared to other halo stars.

As described in Sect. 2.2, symbols in Figs. 3–6 are hatched according to the subgroups discussed by Dodd et al. (2022). Both subgroups show similar abundance peculiarities compared to other halo stars (lower abundances of α-elements and Y). This result supports that both subgroups can be regarded as a part of the Helmi streams. We made a similar inspection between stars with positive and negative v_z and reached the same conclusion.

We note that the only star with an exceptionally high value of E_n (2447_5952) has a slightly different elemental abundance than the other Helmi stream stars. The different behavior of this star is especially prominent in Ca, Ti and neutron-capture elements (Figs. 4 and 6). This might indicate that the Helmi streams do not extend toward high E_n, which is consistent with the recent identification of Helmi stream members based on clustering analysis of halo stars (Lövdal et al. 2022; Ruiz-Lara et al. 2022).

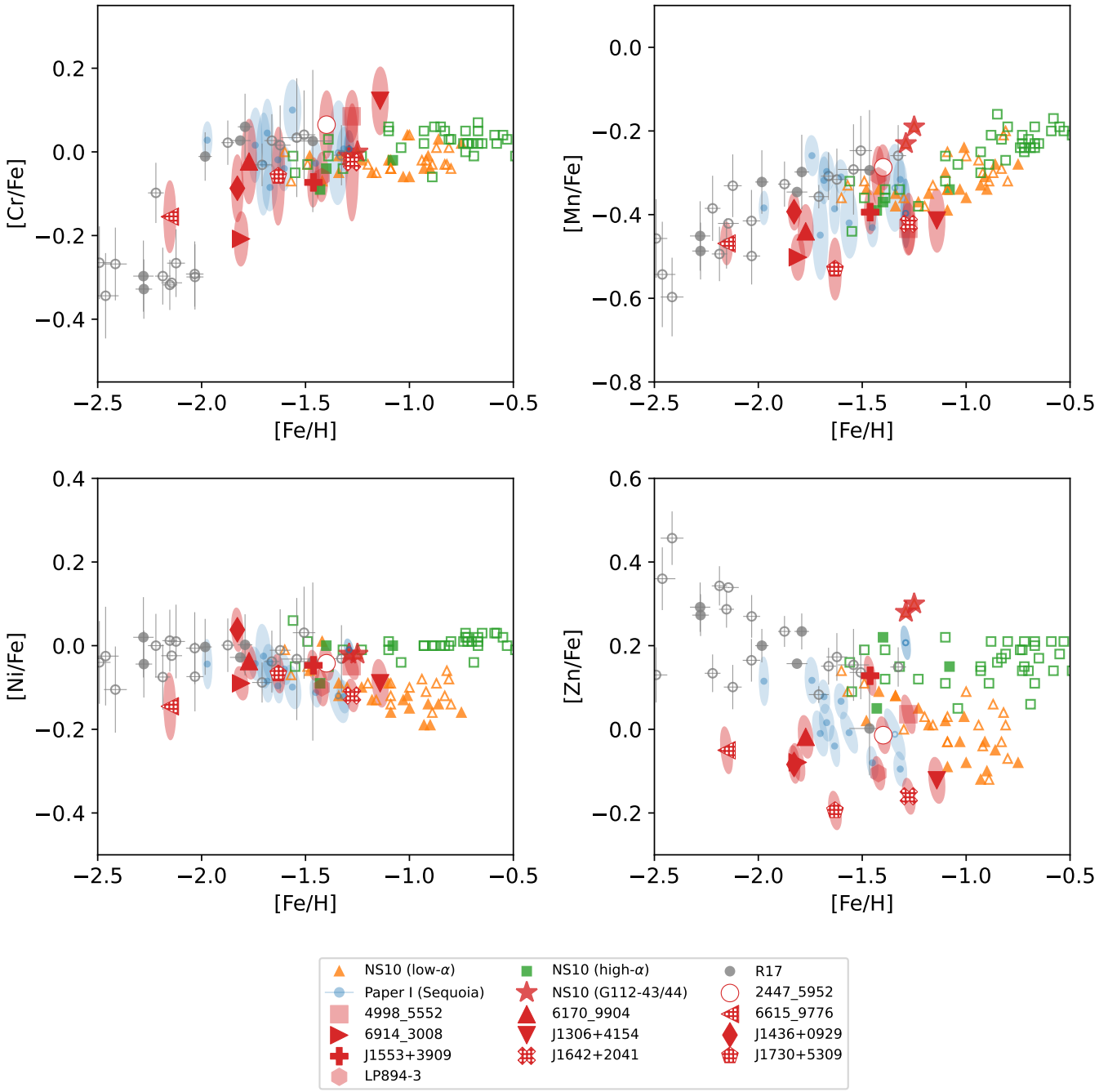

Fig. 5. Abundances of Cr, Mn, Ni, and Zn. Symbols follow Fig. 3.

4. Discussion

4.1. Properties of the Helmi stream progenitor

The chemical properties of the Helmi streams can be summarized as follows. The abundances of elements usually produced by explosions of massive stars (e.g., Na and α-elements) are generally lower than most of the other halo stars, including *Gaia*-Enceladus stars. While the difference to *Gaia*-Enceladus stars becomes less clear at [Fe/H] $\gtrsim -1.5$, the Helmi stream stars still tend to be on the lower side of the distribution in [Mg/Fe], [Ca/Fe], and [Ti/Fe]. Zn and Y also show similar trends as these elements, suggesting they originate in massive stars. This chemical abundance pattern is similar to that seen for Sequoia stars (Paper I).

The low abundance of α-elements and Na are usually attributed to Fe enrichments from type Ia supernovae (SNe Ia). Interestingly, SNe Ia seem to have started to operate in the Helmi stream progenitor already at very low metallicity ([Fe/H] < -2.2) since even the lowest-metallicity star in the sample (6615_9776) has low abundances of α-elements and Na. Assuming that every system has the same abundance ratios among Na, α-elements, and Fe before the onset of SNe Ia, we can tentatively provide an upper limit for the "knee" metallicity as $[\mathrm{Fe/H}]_{\mathrm{knee}} \lesssim -2.4$ from the ~0.2 dex lower [Mg/Fe] of 6615_9776 than the halo stars from R17.

Another interesting feature in α-elements is that there is no apparent decreasing trend in [α/Fe] with metallicity. Moreover, a few stars at [Fe/H] ~ -1.2 seem to have higher [α/Fe] than

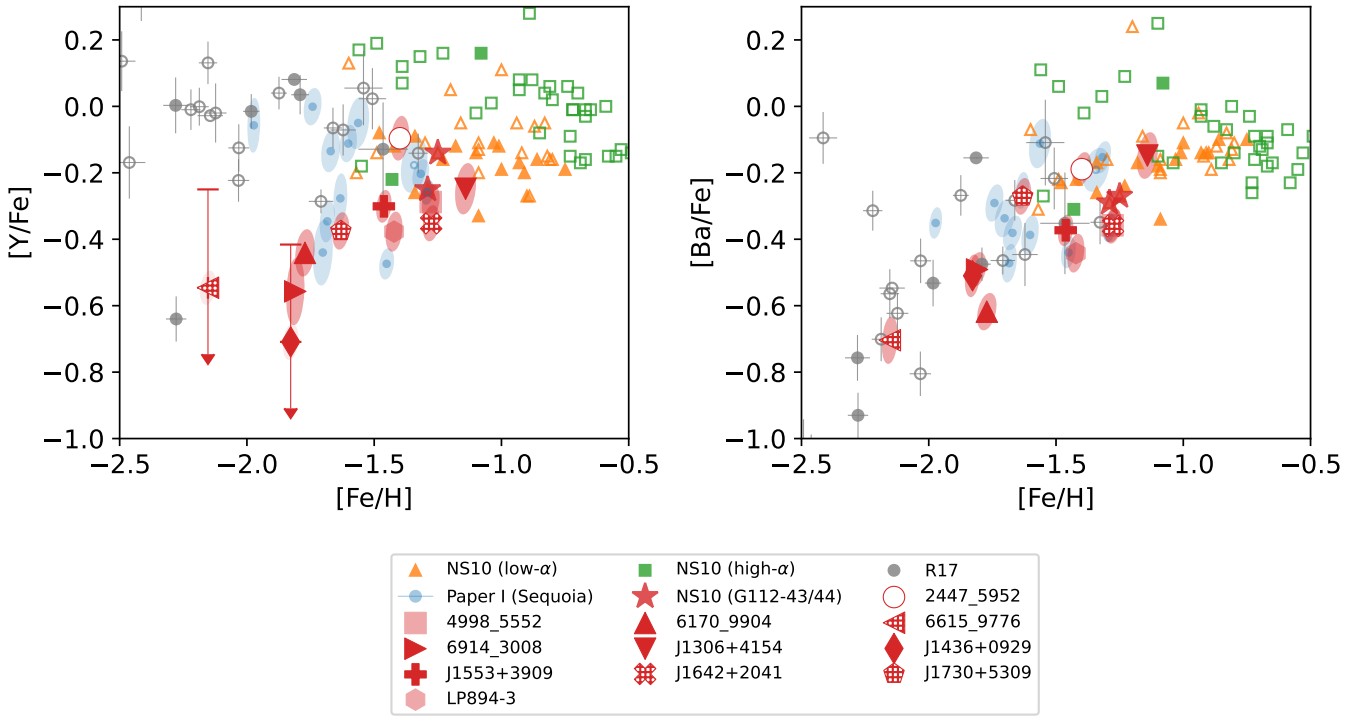

Fig. 6. Abundances of Y and Ba. Symbols follow Fig. 3.

the stars at [Fe/H] ~ -1.8, although it remains to be seen if they are actually the Helmi stream members rather than contaminants from heated thick disk or other accreted populations. If this almost flat or slightly increasing trend is confirmed with a larger sample of homogeneous abundances, it would resemble the observed trend in the Large Magellanic Could (LMC) by Nidever et al. (2020). These authors suggest that such a chemical evolution trend cannot be reproduced in models with a constant star formation efficiency. They suggest that such a trend needs a starburst at a late phase. Although the progenitor of the Helmi streams might have experienced a similar starburst at a late phase, the old age of the majority of the Helmi stream stars (Koppelman et al. 2019; Ruiz-Lara et al. 2022) suggests that the transition from quiescent to bursty star formation occurred on a shorter timescale than that in LMC. A future chemodynamical study with precise stellar age as well as chemical evolution modeling would be necessary to confirm this scenario.

The Y abundance of the Helmi stream stars is particularly low at [Fe/H] $\lesssim -1.8$. Together with the results of Aguado et al. (2021) on Sr abundance, this suggests that the Helmi stream stars have very low abundances of light neutron-capture elements. Such a low light neutron-capture element abundance is not common among the Milky Way stars but is seen in low-mass dwarf galaxies such as Draco and Ursa Minor dwarf spheroids and most of the ultra-faint dwarf galaxies (e.g., Frebel & Norris 2015).

Several nucleosynthesis processes have been proposed as production sites of these light neutron-capture elements, including *r*-process in neutron star mergers (Wanajo et al. 2014; Watson et al. 2019), in magneto-rotational supernovae (Winteler et al. 2012), or in collapsars (Siegel et al. 2019), *s*-process in low- to intermediate-mass stars (Karakas & Lattanzio 2014), weak *s*-process in rapidly rotating massive stars (Frischknecht et al. 2012; Choplin et al. 2018), and weak *r*-process in electron-capture supernovae (Wanajo et al. 2011). It is not yet clear which process is the dominant source of the elements in the early Universe (see discussions by, e.g., Côté et al. 2019; Prantzos et al. 2018; Kobayashi et al. 2020). Since we here discuss the low-metallicity end of the sample, the production of neutron-capture elements would not be dominated by low- to intermediate-mass stars (e.g., de los Reyes et al. 2022). One possible explanation for the low light neutron-capture element abundances of the Helmi streams is that, as a result of the low stellar mass of the galaxy, the progenitor did not experience rare *r*-process nucleosynthesis events, such as neutron star mergers, electron capture supernovae, and magneto-rotational supernovae. In this case, a small amount of light neutron-capture elements could be produced by rapidly rotating massive stars (Hirai et al. 2019; Tarumi et al. 2021). Another explanation is that the progenitor dwarf galaxy had a small number of rotating massive stars. The small number of rotating massive stars might be a result of the top-light initial mass function in dwarf galaxies (Weidner & Kroupa 2005), or different distribution of initial rotation velocity of stars. The observational indication by Gull et al. (2021) that metal-poor stars of the Helmi streams show *r*-process abundance pattern in neutron-capture elements heavier than Ba might favor the second possibility. However, it is necessary to investigate the abundance pattern of light neutron-capture elements in order to understand the cause of the low light neutron-capture element abundance of the Helmi streams. A larger sample of low-metallicity Helmi stream stars with neutron-capture element abundances would also be welcomed. They would enable us to constrain the property of the nucleosynthesis processes, such as their event rates, by studying how neutron-capture elements were enriched as a function of metallicity (e.g., Tsujimoto et al. 2017).

The [Zn/Fe] values observed at high metallicity are also noteworthy. While the binary pair G112-43 and G112-44 have high Zn abundance (Nissen et al. 2021), other Helmi stream stars do not share such a high abundance, resulting in a large

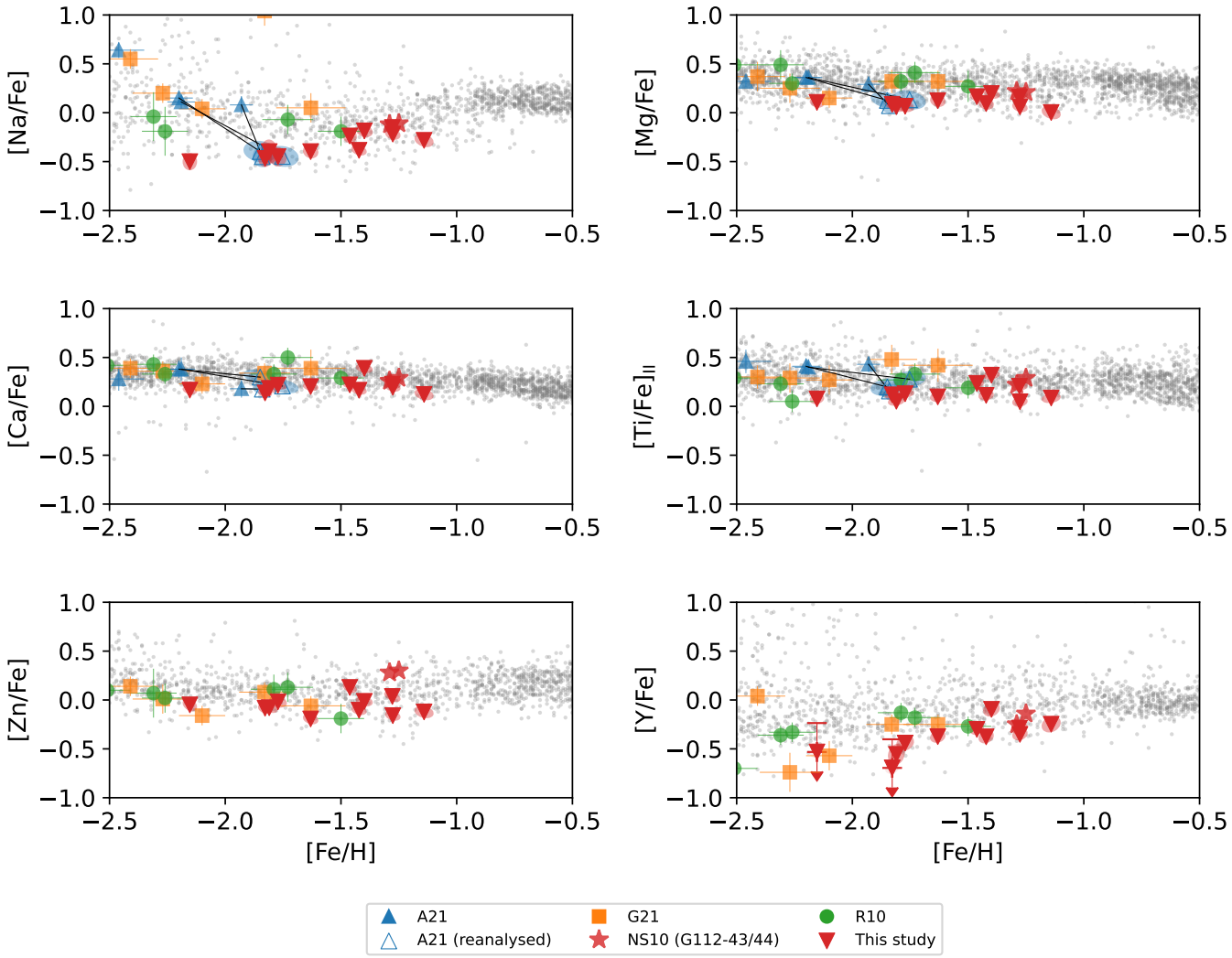

Fig. 7. Chemical abundance of the Helmi stream stars from literature, namely Roederer et al. (R10; 2010), Aguado et al. (A21; 2021), and Gull et al. (G21; 2021). We also include Helmi stream stars in the present study and in NS10. The background gray points are from the SAGA database (Suda et al. 2008, 2011; Yamada et al. 2013). The UVES spectra of three stars from Aguado et al. (2021) were reanalysed and abundances from the reanalysis are included in the figure. Abundances from our reanalysis and those from Aguado et al. (2021) are connected with a solid line for each star.

star-to-star variation in [Zn/Fe]. Although Nissen et al. (2021) noted that the binary pair is also enhanced in Mn, Ni, and Cu, the measurement uncertainties in the present study are not high enough to see if there are significant scatters in Mn and Ni abundances among the Helmi stream stars. A significant dispersion in [Zn/Fe] at high metallicity is also reported in the Sculptor dwarf spheroidal galaxy (Skúladóttir et al. 2017). While Hirai et al. (2018) provided a theoretical calculation of Zn enrichments in dwarf galaxies, assuming electron capture supernovae as one of the sources of Zn, they find it challenging to produce a large scatter at high metallicity. Based on iron-group element abundances, Nissen et al. (2021) suggest pure helium detonation type Ia supernovae could be a promising nucleosynthesis event producing the unique abundance pattern of the binary pair. It remains to be seen whether chemical evolution models including this type of SNe Ia can explain the Zn abundance variation within a galaxy. A larger sample of stars with precise multi-element abundances would be helpful to establish, for example, if the binary pair is a chemical outlier or a tail of [Zn/Fe] distribution in the system and if the Zn abundance correlates with abundances of other elements.

4.2. Helmi streams in the literature

In this section, we highlight the importance of homogeneous chemical abundance through a comparison of our results with those presented in the literature, by Roederer et al. (2010), by Limberg et al. (2021), by Gull et al. (2021), and by Aguado et al. (2021)[6]. All but Limberg et al. (2021) conducted new observations of the Helmi stream stars, while Limberg et al. (2021) used the data from GALAH DR3. All, including Limberg et al. (2021), compared the chemical abundance of the Helmi stream stars with a literature compilation without homogenizing the chemical abundances.

Figure 7 compares the abundances of the Helmi stream stars from those literature studies and from our present work, with those of stars in the Milky Way from various literature sources (SAGA database; Suda et al. 2008, 2011; Yamada et al. 2013). To confirm the membership to the Helmi streams, we recomputed angular momenta of the stars in Roederer et al. (2010), Gull et al. (2021), and Aguado et al. (2021) consistently and res-

[6] We consider five stars observed with high-resolution spectrographs (HORuS and UVES) for the Aguado et al. (2021) sample.

elected the Helmi stream members. As there is no report of radial velocity in Aguado et al. (2021), we adopted radial velocity measurements by SDSS or LAMOST for their stars. For the stars in common between Roederer et al. (2010) and Gull et al. (2021), we prioritized the measurements by the latter study over the former. We also included in the figure abundances that we obtained for three stars studied by Aguado et al. (2021) by reanalyzing their UVES spectra. For this reanalysis, we redetermined stellar parameters following the same procedure as described in Paper I and estimated the abundances using these parameters.

We first emphasize the importance of homogeneity in abundance by using the three stars from Aguado et al. (2021) that we reanalyzed. As can be seen in Fig. 7, stars from Aguado et al. (2021) seem to have higher α-elements abundances compared to the Helmi stream stars in the present study if we adopt the reported abundances. On the other hand, our reanalysis shows that the three stars actually have similar abundances as the sample in the present study, although the uncertainties are larger due to different spectral quality. To investigate the effect of different stellar parameters, we fixed $T_{\rm eff}$ and $\log g$ to the values adopted by Aguado et al. (2021), determined v_t and metallicity, and then measured abundances instead of redetermining the four stellar parameters. The results do not change significantly compared to what we obtained from the full reanalysis. The source of difference thus could be due to different atomic data, line selection, and/or spectral synthesis software.

The different abundance from Aguado et al. (2021) and our reanalysis is not too surprising since it has been known that systematic uncertainty can be significant when abundances from different studies are compared without homogenization. For example, G112-43 is a well studied star and its abundance is available in a number of literature (Ryan et al. 2001; Charbonnel & Primas 2005; Zhang et al. 2009; Ishigaki et al. 2010, 2012, 2013; Nissen & Schuster 2010, 2011; Yan et al. 2016)[7]. The reported metallicity ([Fe/H]$_{\rm I}$) and [Mg/Fe] of this star respectively range from -1.52 (Ishigaki et al. 2010) to -1.14 (Zhang et al. 2009), and from 0.16 (Zhang et al. 2009) to 0.37 (Ishigaki et al. 2010). These ranges are significantly larger than the typical uncertainty reported. We note that we derive [Fe/H]$_{\rm I}$ = -1.254 and [Mg/Fe] = 0.179 in Paper I and NS10 (adopted for figures) derive [Fe/H]$_{\rm I}$ = -1.25 and [Mg/Fe] = 0.21.

Figure 7 demonstrates that our sample has the smallest uncertainty, which was made possible thanks to the high quality of the spectra. However, even with the high precision, the chemical distinctness of the Helmi stream stars is less clear than what we see in Figs. 3–6. This is because the comparison sample from the SAGA database is not necessarily on the same abundance scale as ours, because its distribution is broadened due to systematic uncertainty, and because it can contain poor quality data.

In conclusion, systematic uncertainties have hampered a clear chemical characterization of the Helmi stream stars in previous studies. Thanks to our approach of abundance analysis and homogenization of abundances from literature (see, Paper I), we can detect clear but small abundance difference between the Helmi stream stars and other halo stars that include *Gaia*-Enceladus stars.

5. Summary

Through a differential abundance analysis, we show that the Helmi stream stars clearly depict lower [X/Fe] in Na, Mg, Ca, Ti, Zn, and Y, compared to the other halo stars, including stars accreted from *Gaia*-Enceladus. While the distinction from *Gaia*-Enceladus stars is clearer at [Fe/H] $\lesssim -1.5$, a part of the Helmi stream stars start to overlap with *Gaia*-Enceladus stars in elemental abundance ratios at high metallicities.

This is the first time that we see the chemical distinctness of the Helmi stream stars over a wide metallicity range. This result was made possible thanks to the precise abundances derived in this study and to the homogenization of abundances across NS10, R17 and the present study. As in Paper I, the present investigation of the Helmi streams highlights the importance of homogenized abundances for chemical identification of individual building blocks of the Milky Way.

The observed low α-element abundances of the Helmi streams are likely due to the Fe enrichments from SNe Ia at low metallicity. There seems to be a contribution of SNe Ia to the chemical evolution of the progenitor already at very low metallicity ([Fe/H] $\lesssim -2.4$), indicating that the star formation proceeded with low efficiency in early times. Star formation at later times might have been bursty since [α/Fe] remains almost constant or slightly increases toward high metallicities according to Nidever et al. (2020); such a feature may require a late starburst.

The origin of the extremely low Y abundances at low metallicity remains unclear. Our results, as well as those of Aguado et al. (2021) on Sr, strongly suggest that the Helmi streams have very low abundances of light neutron-capture elements at low metallicity. It would be interesting to obtain detailed abundance patterns over light neutron-capture elements in order to constrain the nucleosynthesis processes that produce this feature.

Further observations would also be able to aid understanding of the Zn abundance variation at high metallicity. The binary pair G112-43 and G112-44 are the only stars with clear Zn enhancements, and all the other Helmi stream stars at [Fe/H] $\gtrsim -1.5$ have Zn abundances comparable to or lower than *Gaia*-Enceladus stars. It would be interesting to investigate the detailed [Zn/Fe] distribution with a lager number of stars.

Acknowledgements. We thank the anonymous referee for his/her constructive comments, which helped us with improving the clarity of the discussion. We thank David Aguado for sharing their UVES spectra with us. This research has been supported by a Spinoza Grant from the Dutch Research Council (NWO). W.A. and M.N.I. were supported by JSPS KAKENHI Grant Number 21H04499. MNI is supported by JSPS KAKENHI Grant Number 20H05855. Z.Y. acknowledges support from the French National Research Agency (ANR) funded project "Pristine" (ANR-18-CE31-0017) and the European Research Council (ERC) under the European Unions Horizon 2020 research and innovation programme (grant agreement No. 834148). This research is based in part on data collected at Subaru Telescope, which is operated by the National Astronomical Observatory of Japan. We are honored and grateful for the opportunity of observing the Universe from Maunakea, which has the cultural, historical and natural significance in Hawaii. Part of the data were retrieved from the JVO portal (`http://jvo.nao.ac.jp/portal/`) operated by ADC/NAOJ.

References

Aguado, D. S., Myeong, G. C., Belokurov, V., et al. 2021, MNRAS, 500, 889
Bennett, M., & Bovy, J. 2019, MNRAS, 482, 1417
Casagrande, L., & VandenBerg, D. A. 2018, MNRAS, 479, L102
Cayrel, R. 1988, in The Impact of Very High S/N Spectroscopy on Stellar Physics, eds. G. Cayrel de Strobel, & M. Spite, 132, 345
Charbonnel, C., & Primas, F. 2005, A&A, 442, 961
Chiba, M., & Beers, T. C. 2000, AJ, 119, 2843
Choplin, A., Hirschi, R., Meynet, G., et al. 2018, A&A, 618, A133
Côté, B., Eichler, M., Arcones, A., et al. 2019, ApJ, 875, 106
de los Reyes, M.A.C., Kirby, E.N., Ji, A.P., & Nuñez, E.H. 2022, ApJ, 925, 66
Dodd, E., Helmi, A., & Koppelman, H. H. 2022, A&A, 659, A61
Frebel, A., & Norris, J. E. 2015, ARA&A, 53, 631
Frischknecht, U., Hirschi, R., & Thielemann, F. K. 2012, A&A, 538, L2

[7] The data are collected through the SAGA database.

Gaia Collaboration (Brown, A. G. A., et al.) 2018, A&A, 616, A1
Gaia Collaboration (Brown, A. G. A., et al.) 2021, A&A, 649, A1
Green, G. M., Schlafly, E., Zucker, C., Speagle, J. S., & Finkbeiner, D. 2019, ApJ, 887, 93
Gull, M., Frebel, A., Hinojosa, K., et al. 2021, ApJ, 912, 52
Gustafsson, B., Edvardsson, B., Eriksson, K., et al. 2008, A&A, 486, 951
Helmi, A., White, S. D. M., de Zeeuw, P. T., & Zhao, H. 1999, Nature, 402, 53
Hirai, Y., Saitoh, T. R., Ishimaru, Y., & Wanajo, S. 2018, ApJ, 855, 63
Hirai, Y., Wanajo, S., & Saitoh, T. R. 2019, ApJ, 885, 33
Ishigaki, M., Chiba, M., & Aoki, W. 2010, PASJ, 62, 143
Ishigaki, M. N., Chiba, M., & Aoki, W. 2012, ApJ, 753, 64
Ishigaki, M. N., Aoki, W., & Chiba, M. 2013, ApJ, 771, 67
Ji, A. P., Li, T. S., Hansen, T. T., et al. 2020, AJ, 160, 181
Karakas, A. I., & Lattanzio, J. C. 2014, PASA, 31, e030
Kepley, A. A., Morrison, H. L., Helmi, A., et al. 2007, AJ, 134, 1579
Kobayashi, C., Karakas, A. I., & Lugaro, M. 2020, ApJ, 900, 179
Koppelman, H., Helmi, A., & Veljanoski, J. 2018, ApJ, 860, L11
Koppelman, H. H., Helmi, A., Massari, D., Roelenga, S., & Bastian, U. 2019, A&A, 625, A5
Limberg, G., Santucci, R. M., Rossi, S., et al. 2021, ApJ, 913, L28
Lind, K., Asplund, M., Barklem, P. S., & Belyaev, A. K. 2011, A&A, 528, A103
Lövdal, S. S., Ruiz-Lara, T., Koppelman, H. H., et al. 2022, A&A, in press, https://doi.org/10.1051/0004-6361/202243060
Matsuno, T., Koppelman, H. H., Helmi, A., et al. 2022, A&A, 661, A103
McMillan, P. J. 2017, MNRAS, 465, 76
Myeong, G. C., Evans, N. W., Belokurov, V., Amorisco, N. C., & Koposov, S. E. 2018, MNRAS, 475, 1537
Nidever, D. L., Hasselquist, S., Hayes, C. R., et al. 2020, ApJ, 895, 88
Nissen, P. E., & Schuster, W. J. 2010, A&A, 511, L10
Nissen, P. E., & Schuster, W. J. 2011, A&A, 530, A15
Nissen, P. E., Silva-Cabrera, J. S., & Schuster, W. J. 2021, A&A, 651, A57
Noguchi, K., Aoki, W., Kawanomoto, S., et al. 2002, PASJ, 54, 855
Prantzos, N., Abia, C., Limongi, M., Chieffi, A., & Cristallo, S. 2018, MNRAS, 476, 3432
Reggiani, H., Meléndez, J., Kobayashi, C., Karakas, A., & Placco, V. 2017, A&A, 608, A46
Reid, M. J., & Brunthaler, A. 2004, ApJ, 616, 872
Roederer, I. U., Sneden, C., Thompson, I. B., Preston, G. W., & Shectman, S. A. 2010, ApJ, 711, 573
Ruiz-Lara, T., Matsuno, T., Sofie Lövdal, S., et al. 2022, A&A, in press, https://doi.org/10.1051/0004-6361/202243061
Ryan, S. G., Kajino, T., Beers, T. C., et al. 2001, ApJ, 549, 55
Schlegel, D. J., Finkbeiner, D. P., & Davis, M. 1998, ApJ, 500, 525
Schönrich, R., Binney, J., & Dehnen, W. 2010, MNRAS, 403, 1829
Siegel, D. M., Barnes, J., & Metzger, B. D. 2019, Nature, 569, 241
Skúladóttir, Á., Tolstoy, E., Salvadori, S., Hill, V., & Pettini, M. 2017, A&A, 606, A71
Sneden, C. 1973, ApJ, 184, 839
Suda, T., Katsuta, Y., Yamada, S., et al. 2008, PASJ, 60, 1159
Suda, T., Yamada, S., Katsuta, Y., et al. 2011, MNRAS, 412, 843
Tajitsu, A., Aoki, W., & Yamamuro, T. 2012, PASJ, 64, 77
Tarumi, Y., Suda, T., van de Voort, F., et al. 2021, MNRAS, 505, 3755
Tsujimoto, T., Matsuno, T., Aoki, W., Ishigaki, M. N., & Shigeyama, T. 2017, ApJ, 850, L12
Wanajo, S., Janka, H.-T., & Müller, B. 2011, ApJ, 726, L15
Wanajo, S., Sekiguchi, Y., Nishimura, N., et al. 2014, ApJ, 789, L39
Watson, D., Hansen, C. J., Selsing, J., et al. 2019, Nature, 574, 497
Weidner, C., & Kroupa, P. 2005, ApJ, 625, 754
Winteler, C., Käppeli, R., Perego, A., et al. 2012, ApJ, 750, L22
Yamada, S., Suda, T., Komiya, Y., Aoki, W., & Fujimoto, M. Y. 2013, MNRAS, 436, 1362
Yan, H. L., Shi, J. R., Nissen, P. E., & Zhao, G. 2016, A&A, 585, A102
Zhang, L., Ishigaki, M., Aoki, W., Zhao, G., & Chiba, M. 2009, ApJ, 706, 1095

Appendix A: Additional table

Table A.1. Abundances of the Helmi stream stars

	2447_5952					4998_5552					6170_9904				
	N	[X/H]	σ	[X/Fe]	σ	N	[X/H]	σ	[X/Fe]	σ	N	[X/H]	σ	[X/Fe]	σ
FeI	103	-1.399	0.032	...	...	88	-1.278	0.031	...	...	93	-1.772	0.034	...	...
FeII	12	-1.420	0.025	...	...	13	-1.268	0.042	...	...	11	-1.733	0.025	...	...
NaI	3	-1.585	0.055	-0.186	0.054	2	-1.430	0.041	-0.152	0.039	2	-2.222	0.093	-0.450	0.089
MgI	7	-1.202	0.041	0.196	0.042	4	-1.119	0.040	0.159	0.038	5	-1.706	0.052	0.066	0.050
SiI	2	-1.077	0.051	0.322	0.054	6	-0.973	0.046	0.305	0.052	0	<-1.727(-1.517)		<0.045(0.255)	
CaI	19	-1.010	0.041	0.389	0.038	18	-1.051	0.044	0.227	0.040	19	-1.555	0.038	0.217	0.035
TiI	11	-1.063	0.067	0.336	0.058	15	-1.184	0.053	0.094	0.044	8	-1.528	0.066	0.244	0.056
TiII	13	-1.102	0.041	0.319	0.033	8	-1.064	0.043	0.205	0.039	12	-1.604	0.035	0.129	0.033
CrI	4	-1.334	0.087	0.065	0.080	2	-1.193	0.070	0.085	0.061	3	-1.796	0.106	-0.023	0.100
MnI	5	-1.686	0.060	-0.287	0.053	7	-1.712	0.068	-0.434	0.062	5	-2.212	0.071	-0.440	0.063
NiI	14	-1.441	0.045	-0.042	0.040	22	-1.327	0.031	-0.049	0.031	8	-1.810	0.047	-0.037	0.042
ZnI	2	-1.412	0.047	-0.014	0.043	2	-1.242	0.037	0.036	0.045	2	-1.790	0.052	-0.018	0.050
YII	2	-1.516	0.069	-0.096	0.064	2	-1.556	0.047	-0.288	0.049	1	-2.174	0.069	-0.441	0.068
BaII	4	-1.610	0.058	-0.189	0.048	4	-1.627	0.049	-0.358	0.048	4	-2.351	0.055	-0.618	0.053
	6615_9776					6914_3008					J1306+4154				
	N	[X/H]	σ	[X/Fe]	σ	N	[X/H]	σ	[X/Fe]	σ	N	[X/H]	σ	[X/Fe]	σ
FeI	92	-2.153	0.027	...	...	95	-1.810	0.032	...	...	102	-1.141	0.037	...	...
FeII	5	-2.183	0.030	...	...	11	-1.737	0.027	...	...	13	-1.214	0.030	...	...
NaI	2	-2.654	0.083	-0.501	0.078	3	-2.208	0.116	-0.398	0.114	3	-1.424	0.059	-0.283	0.059
MgI	5	-2.048	0.046	0.106	0.044	7	-1.750	0.042	0.061	0.042	7	-1.140	0.059	0.002	0.059
SiI	0	<-1.894(-1.653)		<0.258(0.499)		1	-1.334	0.079	0.476	0.082	3	-1.007	0.087	0.134	0.090
CaI	18	-1.988	0.034	0.166	0.033	19	-1.626	0.039	0.184	0.036	17	-1.020	0.051	0.122	0.049
TiI	8	-2.117	0.064	0.037	0.056	10	-1.769	0.069	0.041	0.059	11	-1.027	0.082	0.115	0.075
TiII	10	-2.107	0.034	0.076	0.042	9	-1.684	0.029	0.052	0.036	11	-1.129	0.042	0.085	0.041
CrI	2	-2.308	0.090	-0.155	0.085	3	-2.018	0.073	-0.208	0.064	5	-1.020	0.089	0.122	0.080
MnI	2	-2.623	0.056	-0.469	0.050	4	-2.313	0.062	-0.502	0.054	6	-1.556	0.083	-0.414	0.075
NiI	5	-2.298	0.081	-0.145	0.079	12	-1.900	0.042	-0.090	0.039	13	-1.231	0.060	-0.090	0.056
ZnI	2	-2.203	0.052	-0.050	0.055	2	-1.889	0.040	-0.079	0.044	2	-1.263	0.057	-0.122	0.054
YII	0	<-2.729(-2.433)		<-0.546(-0.250)		1	-2.294	0.095	-0.557	0.098	2	-1.462	0.074	-0.248	0.074
BaII	2	-2.887	0.062	-0.704	0.068	4	-2.228	0.043	-0.491	0.049	4	-1.362	0.069	-0.148	0.067
	J1436+0929					J1553+3909					J1642+2041				
	N	[X/H]	σ	[X/Fe]	σ	N	[X/H]	σ	[X/Fe]	σ	N	[X/H]	σ	[X/Fe]	σ
FeI	88	-1.828	0.026	...	...	74	-1.462	0.026	...	...	103	-1.276	0.029	...	...
FeII	8	-1.822	0.038	...	...	9	-1.410	0.027	...	...	15	-1.249	0.044	...	...
NaI	2	-2.296	0.082	-0.468	0.077	4	-1.700	0.068	-0.238	0.066	3	-1.495	0.049	-0.219	0.048
MgI	6	-1.742	0.047	0.086	0.044	4	-1.298	0.041	0.164	0.039	6	-1.216	0.045	0.060	0.044
SiI	0	<-1.355(-1.203)		<0.472(0.624)		2	-1.128	0.051	0.334	0.054	3	-1.242	0.056	0.034	0.057
CaI	13	-1.691	0.034	0.137	0.031	12	-1.241	0.033	0.220	0.030	16	-1.080	0.038	0.196	0.036
TiI	7	-1.609	0.050	0.219	0.041	14	-1.361	0.054	0.101	0.046	10	-1.262	0.064	0.014	0.056
TiII	12	-1.704	0.039	0.118	0.049	2	-1.175	0.039	0.235	0.041	10	-1.202	0.051	0.047	0.041
CrI	2	-1.915	0.084	-0.087	0.079	3	-1.535	0.065	-0.073	0.058	2	-1.301	0.142	-0.025	0.139
MnI	3	-2.221	0.049	-0.393	0.043	4	-1.856	0.056	-0.394	0.051	5	-1.698	0.077	-0.422	0.072
NiI	5	-1.790	0.053	0.038	0.051	18	-1.509	0.038	-0.047	0.035	12	-1.395	0.041	-0.119	0.038
ZnI	2	-1.912	0.045	-0.084	0.044	2	-1.333	0.041	0.128	0.046	2	-1.436	0.042	-0.160	0.042
YII	0	<-2.531(-2.238)		<-0.709(-0.416)		2	-1.711	0.042	-0.301	0.046	2	-1.601	0.056	-0.352	0.051
BaII	3	-2.332	0.052	-0.510	0.061	4	-1.783	0.043	-0.373	0.044	4	-1.609	0.057	-0.360	0.050
	J1730+5309					LP894-3									
	N	[X/H]	σ	[X/Fe]	σ	N	[X/H]	σ	[X/Fe]	σ					
FeI	84	-1.631	0.029	...	...	98	-1.422	0.029	...	...					
FeII	12	-1.643	0.039	...	...	14	-1.488	0.033	...	...					
NaI	3	-2.029	0.062	-0.398	0.059	3	-1.807	0.043	-0.385	0.043					
MgI	6	-1.508	0.057	0.123	0.054	6	-1.329	0.055	0.093	0.052					
SiI	0	<-1.497(-1.352)		<0.133(0.278)		4	-1.243	0.062	0.179	0.063					
CaI	16	-1.429	0.037	0.202	0.034	18	-1.257	0.039	0.165	0.036					
TiI	8	-1.523	0.055	0.108	0.045	10	-1.348	0.066	0.074	0.058					
TiII	9	-1.546	0.049	0.097	0.042	7	-1.376	0.037	0.112	0.042					
CrI	2	-1.689	0.121	-0.058	0.116	4	-1.482	0.066	-0.060	0.058					
MnI	7	-2.161	0.078	-0.530	0.073	3	-1.730	0.074	-0.308	0.070					
NiI	9	-1.698	0.047	-0.067	0.045	16	-1.522	0.046	-0.100	0.043					
ZnI	2	-1.825	0.045	-0.194	0.045	2	-1.527	0.040	-0.105	0.039					
YII	2	-2.018	0.057	-0.375	0.053	2	-1.865	0.055	-0.377	0.057					
BaII	3	-1.914	0.057	-0.271	0.052	4	-1.929	0.054	-0.442	0.055					

Notes. For upper limits, we provide both 1-σ and 3-σ upper limits. The values in parenthesis are for the 3-σ upper limits.